IOP Publishing Smart Materials and Structures
Smart Mater. Struct. 24 (2015) 035012 (13pp) doi:10.1088/0964-1726/24/3/035012

Nonlinear geometric influence on the mechanical behavior of shape memory alloy helical springs

Marcelo A Savi[1,3], Pedro Manuel C L Pacheco[2], Mauricio S Garcia[1], Ricardo A A Aguiar[2], Luís Felipe G de Souza[2] and Rodolpho B da Hora[2]

[1] Universidade Federal do Rio de Janeiro, COPPE, Department of Mechanical Engineering, PO Box 68.503, 21.941.972, Rio de Janeiro, RJ, Brazil
[2] CEFET/RJ—Centro Federal de Educação Tecnológica Celso Suckow da Fonseca, Department of Mechanical Engineering, 20.271.110, Rio de Janeiro, RJ, Brazil

E-mail: savi@mecanica.ufrj.br, calas@cefet-rj.br, mauriciogarc@gmail.com, raaguiar@cefet-rj.br, lfelipe@cefet-rj.br and rodolphodahora@gmail.com

Received 18 July 2014, revised 16 December 2014
Accepted for publication 5 January 2015
Published 6 February 2015

Abstract

This paper investigates the nonlinear geometric effect on the mechanical behavior of shape memory alloy (SMA) helical springs. First, the SMA wires are characterized, and then the design and fabrication of SMA helical springs are discussed. Experimental tensile tests are carried out to show the nonlinear geometric influence. Results show a coupling between constitutive and geometric nonlinearities that defines the spring stiffness. Two springs with different geometries are built from SMA wires to define springs with both weak and strong nonlinear geometric influence. Numerical analyses are developed, using the finite element method to confirm the general conclusions shown in our experimental observations.

Keywords: shape memory alloys, pseudoelasticity, spring, geometric nonlinearities

(Some figures may appear in colour only in the online journal)

1. Introduction

Shape memory alloys (SMAs) have been studied since the 1930s, but technological interest in these materials came to the forefront in 1962, when research at the US Naval Ordinance Laboratory discovered the shape memory effect in NiTi alloys. Since then, several industrial applications have been established in areas such as aeronautics, medicine, and robotics. SMA actuators are currently being used as an alternative to electric, hydraulic, and pneumatic actuators, and they also fill a growing need to develop smaller and lighter systems. In this regard, the use of SMAs is increasing in different fields of human knowledge due to their good power-to-weight ratios.

SMAs present complex thermomechanical behaviors related to different physical processes. The most common phenomena presented by these materials are pseudoelasticity, the shape memory effect—which may be one-way or two-way—and phase transformation due to temperature variation. In addition to these phenomena, there are more complicated effects that significantly influence their overall thermomechanical behavior, including plastic behavior, tension-compression asymmetry, plastic-phase transformation coupling, transformation induced plasticity, and thermomechanical couplings (Paiva *et al* 2005, Paiva and Savi 2006, Lagoudas 2008). All of these aspects confer the remarkable properties of SMAs that are attracting so much technological interest and motivating different applications in multiple fields of science and engineering (Machado and Savi 2003, Bundhoo *et al* 2009, Hartl *et al* 2010 2010a, Spinella and Dragoni 2010, Min An *et al* 2012).

The unique properties of SMAs result from solid phase transformations that can be induced either by stresses or by temperature. SMA elements can be designed using wires,

[3] Author to whom any correspondence should be addressed.

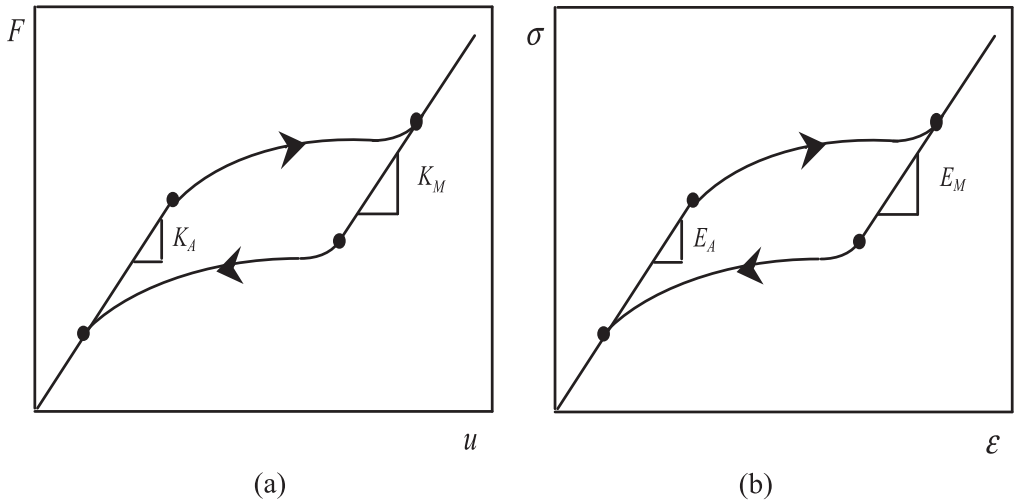

Figure 1. SMA macroscopic pseudoelastic behavior represented by a force-displacement curve for (a) springs, and (b) the stress-strain curve for wires or bars.

beams, and plates, among other possibilities. Hybrid composites allow one to combine the properties of different materials. SMA springs constitute an alternative for applications where large displacements are needed; this is of special relevance in dynamical applications. A mechanical helical spring may be defined as a body with the ability to bend, warp, or absorb energy when subjected to a load (Shigley and Mischke 2001).

The macroscopic mechanical behavior of SMA springs is better expressed by force-displacement (F-u) curves, which have similar characteristics to the stress-strain (σ-ε) curves associated with tensile tests of wires and bars. Figure 1 presents schematic pictures of both curves, showing classical pseudoelastic behavior. One can see a linear elastic region, associated with the austenitic phase, followed by phase transformation plateaus. Afterward, there is a new linear elastic region associated with the martensitic phase. The slope of each linear region of the stress-strain curve defines the elastic modulus. Analogously, the slope of the linear region of the force-displacement curve defines the spring stiffness. Hence, two different parameters are usually defined: E_A and E_M, which are the austenitic and martensitic elastic modulus of wires or bars, respectively, and K_A and K_M, which are the austenitic and martensitic spring element stiffness, respectively. This general behavior is the same for other stress components and can be observed in torsion tests, defining the shear elastic modulus. Usually, SMAs have an austenitic elastic modulus that can be four times greater than the martensitic modulus. Nevertheless, the stiffness of SMA helical springs is affected by the coupling of constitutive and geometrical nonlinearity effects, which introduce changes in the usual mechanical description. The main goal of this paper is to establish a proper comprehension of the geometrical nonlinear effect on helical springs, which is mainly expressed by the spring's stiffness.

SMA springs have been addressed in different forms in the literature. Follador *et al* (2012) pointed out that there are three key aspects related to the design and manufacturing of SMA springs: modeling of the mechanical performance, modeling of the thermomechanical cycles that occur during heating and cooling of the material, and the design of the electric current control. These researchers investigated manufacturing procedures to build springs from wires. Basically, these procedures consist of a mechanical conformation of the spring and a subsequent heat treatment for 30 min at 450 °C in a furnace, followed by a cooling process in a water medium.

Attanasi *et al* (2011) investigated the behavior of pseudoelastic SMA springs to verify the feasibility of their use in devices where the restitution force exceeds the linear limit. Experimental tests were conducted to consider prescribed displacements. In general, procedures for training SMAs consider thermally induced process that occurs when the alloy is heated to temperatures of approximately 500 °C in a time interval of 10 to 25 min.

Mathematical modeling of the thermomechanical behavior of SMA helical springs is also the objective of several research papers. Tobushi and Tanaka (1991) proposed a simplified model where each small segment of the pure spring is subjected to torsion. Liang and Rogers (1997) proposed a nonlinear thermomechanical model for springs used in vibration control. Toi *et al* (2004) presented a model using finite element formulation of the Timoshenko beam and Brinson's model for SMA description. Aguiar *et al* (2010) developed a model for an SMA spring based on the model proposed by Paiva *et al* (2005). Numerical simulations were in close agreement with experimental data for different temperatures. Sung-Min *et al* (2012) developed a simplified model considering both austenite and martensite state and analyzed some geometric effects, such as reducing the diameter of the spring.

This work uses experimental and numerical approaches to investigate the nonlinear geometric influence on the mechanical behavior of SMA helical springs. Two different springs built with distinct geometrical characteristics are designed to change the phase transformation conditions. Both springs are produced from the same SMA wire. The main

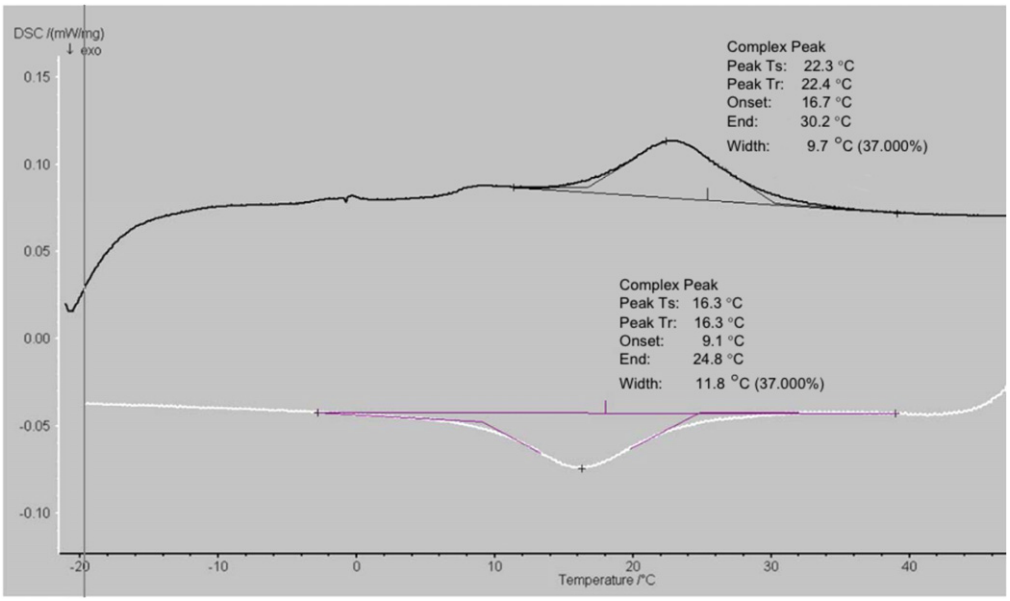

Figure 2. DSC test: phase transformation temperatures.

point is that one spring presents phase transformation related to small displacements, while the other presents large displacements. A comparison is presented between the results of both springs subjected to tensile tests, establishing a proper understanding of geometric influence. Finite element analysis is used to confirm the experimental observations.

This paper is organized as follows. First, the SMA wires are characterized by considering differential scanning calorimeter (DSC) and tensile tests. The training process is an important aspect of this investigation. Then, spring design and fabrication, manufacturing procedures, and heat treatment are examined. Experimental tests of the two springs are then analyzed through tensile tests. Numerical simulations using the finite element method are carried out, confirming the most important conclusions. Finally, concluding remarks are presented.

2. SMA wire

This section discusses the experimental characterization of an SMA wire. NiTi wires of 1.7 mm (0.066 in) are used. DSC and tensile tests are presented. The training process is also shown.

The SMA characterization starts from the determination of phase transformation temperatures. Austenite-martensite and reverse transformation are associated with the release or absorption of latent heat, respectively, which can be measured by the DSC. Figure 2 shows a typical calorimeter measurement. It shows the energy required to maintain the prescribed temperature history of the sample. The upper curve represents a temperature increase, and therefore, transformation from martensite to austenite. These curves define temperatures—A_s and A_f, respectively—as the start and finish of the austenite transformation. On the other hand, the lower curve shows the austenite-martensite transformation, defining the temperatures M_s and M_f as the start and finish of the martensite transformation. The analysis of these curves defines $A_s = 16.7$ °C, $A_f = 30.2$ °C, $M_s = 24.8$ °C, and $M_f = 9.1$ °C.

The next step of SMA characterization is related to tensile tests. MTS Insight 30EL hydraulic test frames with 30 kN load cells, 0.001 mm of position resolution, and 0.01 mm of position accuracy are used, along with a coupled wire extensometer.

Transformation-induced plasticity (TRIP) is a strain mechanism related to the internal stresses that result from the volume and shape changes associated with the phase transformation (Marketz and Fischer 1994). TRIP is a type of irreversible strain that occurs inside the yield surface. This phenomenon is associated with a saturation behavior of SMAs, where stress-strain curves present a movement until it reaches a stabilized behavior. Therefore, it is important to subject the specimen to a training process that can stabilize the stress-strain curve. This training process considers several loading cycles. Figure 3 presents a training process where the SMA sample is subjected to 20 cycles, reaching a maximum value of 2.5 kN load at 60 °C. Note that the stress-strain curves tend to stabilize after several cycles.

After the training process, pseudoelastic tests can define different characteristics of SMA behavior. Temperature dependence is an important aspect to be considered. Hence, tests at different temperature levels can define characteristics such as the phase transformation stress level. In this regard, four stress levels are defined at each temperature: σ_{Ms} and σ_{Mf}, the start and finish of the martensite transformation, and σ_{As} and σ_{Af}, the start and finish of the austenite transformation. Other mechanical properties can also be evaluated from tensile tests. Young's modulus is an essential property, and at room temperature, the following values are estimated: $E_A = 46$ GPa, $E_M = 22$ GPa. Table 1 summarizes all mechanical properties evaluated for the SMA wire, where σ_{rup} and ε_{rup} are the rupture stress and the rupture strain, respectively.

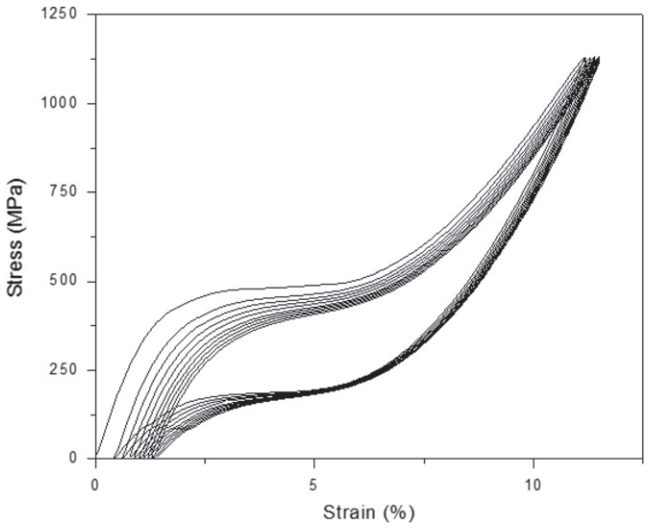

Figure 3. Training process of 20 cycles, reaching the maximum value of 2.5 kN load at 60 °C.

Table 1. Mechanical properties of the SMA wire at room temperature.

Material parameters	E_A (GPa)	E_M (GPa)	σ_{rup} (GPa)	ε_{rup} (%)
NiTi	46	22	1.4	10.0

Based on these properties, it is possible to observe a difference of around 50% between both elastic moduli. The shear modulus is defined as $G = E/2(1 + \nu)$, where ν is the Poisson ratio. Note that there is a direct relation between the elastic and shear moduli. By assuming a Poisson ratio of 0.3, it is possible to estimate the shear modulus: $G_A = 17.7$ and $G_M = 8.5$.

3. SMA helical spring

This section presents a discussion about design, fabrication, and tensile tests of helical springs. Two different springs are built from SMA wires. One spring has a weak influence of geometric nonlinearities, while the other has a strong influence. Basically, geometric nonlinearity is directly related to spring displacement. Hence, the idea is to produce two springs that present different displacements for the same loading level.

3.1. Helical spring design and manufacturing

A spring is a highly flexible mechanical element that is usually used to store and release energy. Helical springs resist and deflect under tensile or compressive loads (Shigley 1986). Essentially, helical springs transform axial force into torque and shear stress in the cross section of the spring. Three geometric parameters are usually considered for the design of a helical spring: wire diameter, d, average coil diameter, D, and the number of active coils, N. Geometric nonlinear effects can dramatically change helical spring behavior when subjected to large displacements. This behavior affects an important design parameter known as the spring index, which establishes a relationship between the coil and wire diameters, $C = D/d$.

Table 2. Spring parameters.

Parameters	W-Spring	S-Spring
Wire diameter (mm)	1.7	1.7
Coil diameter (mm)	10.5	13.8
Spring index (C)	6.2	8.1
Number of active coils	3	5

In contrast with elastic helical springs, SMA helical springs present a nonlinear distribution of shear stress due to phase transformations. This behavior tends to produce even higher displacements when compared to elastic helical springs. Sung-Min *et al* (2012) presented a model considering only two states: martensite and austenite. Based on that, all intermediate phenomena are neglected and only maximum force and displacements are of concern. Under this assumption, a linear approach can be used and the force, F, can be described by a linear relation with the displacement, u, as follows:

$$F = \frac{Gd^4}{8D^3N}\, u \tag{1}$$

This aims to produce two SMA helical springs that present different nonlinear geometric characteristics. The first one, called the W-Spring, has weak geometric nonlinearity, while the second one, called the S-Spring, has a strong geometric influence. The linear approach is used to define the spring's characteristics (Sung-Min *et al* 2012). The idea is to produce both small and large displacements for the same loading level. Table 2 summarizes the characteristics of both springs.

SMA helical spring manufacturing considers an SMA wire that is used to build the spring with the aid of a device where shape is conformed, clamping the spring ends. Then, it is necessary to promote a heat treatment that defines the spring form as a natural one. This treatment is designed to promote SMA recrystallization, assuring proper manufacturing of the spring. Different heat treatments can produce springs with distinct thermomechanical behaviors. For instance, it is possible to produce both an SMA spring with shape memory effect characteristics—meaning that room temperature is less than M_f—and an SMA wire with pseudoelastic characteristics, which means that room temperature is greater than A_f. This kind of situation illustrates the necessity of defining a proper heat treatment.

Jee *et al* (2008) produced an SMA spring built with a NiTi wire with an 0.8 mm diameter, using a heat treatment at 550 °C for 30 min. Morgan and Broadley (2004) discussed several tests to define proper heat treatments. They claimed that typical heat treatments are carried out at temperatures

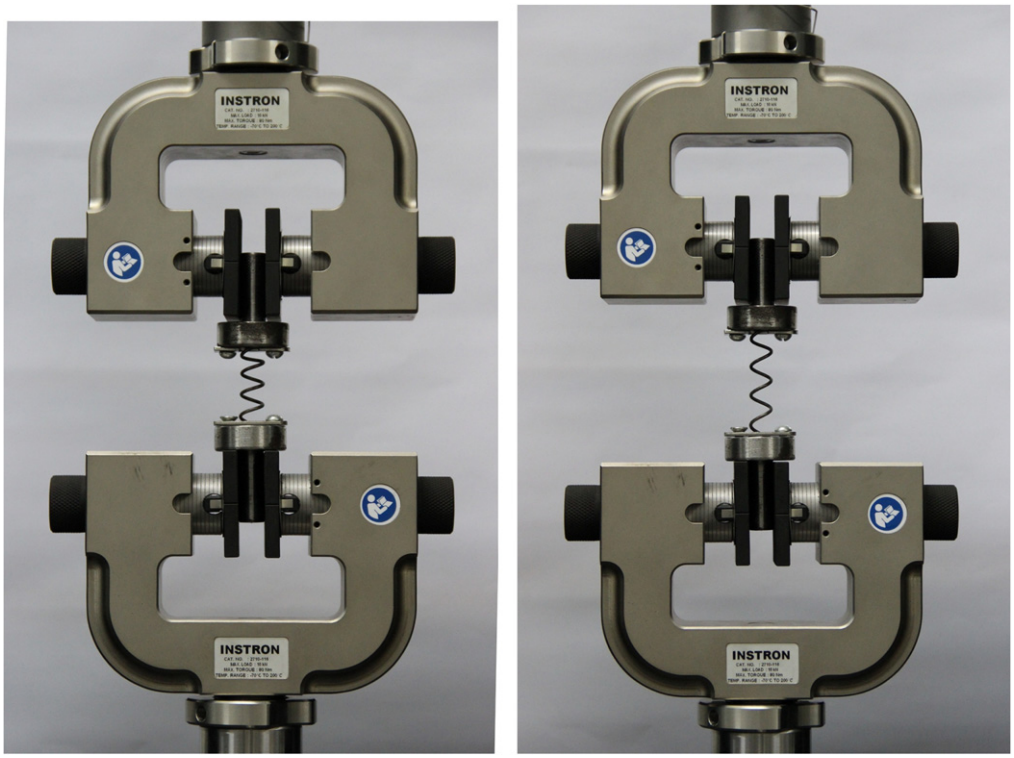

Figure 4. W-Spring test at the maximum displacement configuration: (a) 25 mm, (b) 40 mm.

between 450 °C and 550 °C. Wu (2001) confirmed the recommendation to perform heat treatments close to 500 °C. Other authors recommend a sequence of heat treatments, defining different temperatures and times in the oven to establish the proper thermomechanical behavior of the spring.

Here, three different test temperatures are considered: 450 °C, 500 °C, and 550 °C. Three different treatment times in the oven are also investigated: 10 min, 20 min, and 30 min. After some tests, it is assumed the sample heated at 500 °C for 30 min and, in the experimental sequence, water cooling is performed. Air cooling can generate springs that exhibit the shape memory effect.

3.2. Tensile tests

Tensile tests are performed to characterize the pseudoelastic behavior of SMA helical springs, considering both the W-Spring and S-Spring. Different test scenarios are conducted considering distinct maximum displacements for the same loading level—W-Spring: 5 mm, 10 mm, 25 mm, 30 mm, 35 mm, and 40 mm; S-Spring: 30 mm, 45 mm, 65 mm, 80 mm, 100 mm, and 120 mm. An INSTRON 5966 testing system with 10 kN capacity equipped with a 1 kN load cell is used, considering that the prescribed displacement loading varies from zero to a maximum displacement value using a triangular shape wave with a loading rate of 100 mm min^{-1}. Figure 4 presents pictures of the W-Spring and figure 5 shows the S-Spring.

Stiffness is considered as the essential characteristic of the spring. It is defined from the slope of the linear elastic regions observed before (austenitic phase) and after (martensitic phase) the hysteresis plateau related to the stabilized experimental pseudoelastic curves. The stiffness associated with the austenitic phase is estimated during the loading stage, considering points in the region from 12% to 20% of the maximum load. On the other hand, the stiffness associated with the martensite phase is obtained during the unloading stage, considering points in the region from 90% to 98% of the maximum load. This methodology reduces the influence of instability effects related to the load inversion stage.

First, tensile tests of the W-Spring are presented. Figure 6 shows force-displacement curves for different loadings. The pseudoelastic response of the spring is evident, showing the hysteretic behavior. Although the system has nonlinear characteristics, it is possible to use stiffness related to the austenitic and martensitic phases to define mechanical aspects of the spring. Basically, the slope of the linear elastic regions before and after the hysteresis plateau was considered to be related to the austenitic and martensitic phases, respectively. Note that the slope of the elastic response at the austenitic phase is larger than the one in the martensitic phase. Table 3 presents the summary of the stiffness, showing the average values of $\bar{K}_A = 9.0\,\text{N mm}^{-1}$ and $\bar{K}_M = 4.4\,\text{N mm}^{-1}$. This represents a decrease of around 50%, which is the same amount of the difference of the shear modulus.

Next, tests related to the S-Spring are discussed. Figure 7 shows force-displacement curves related to this spring. The pseudoelastic response is observed again, but this spring has a strong nonlinear geometric influence that causes the opposite

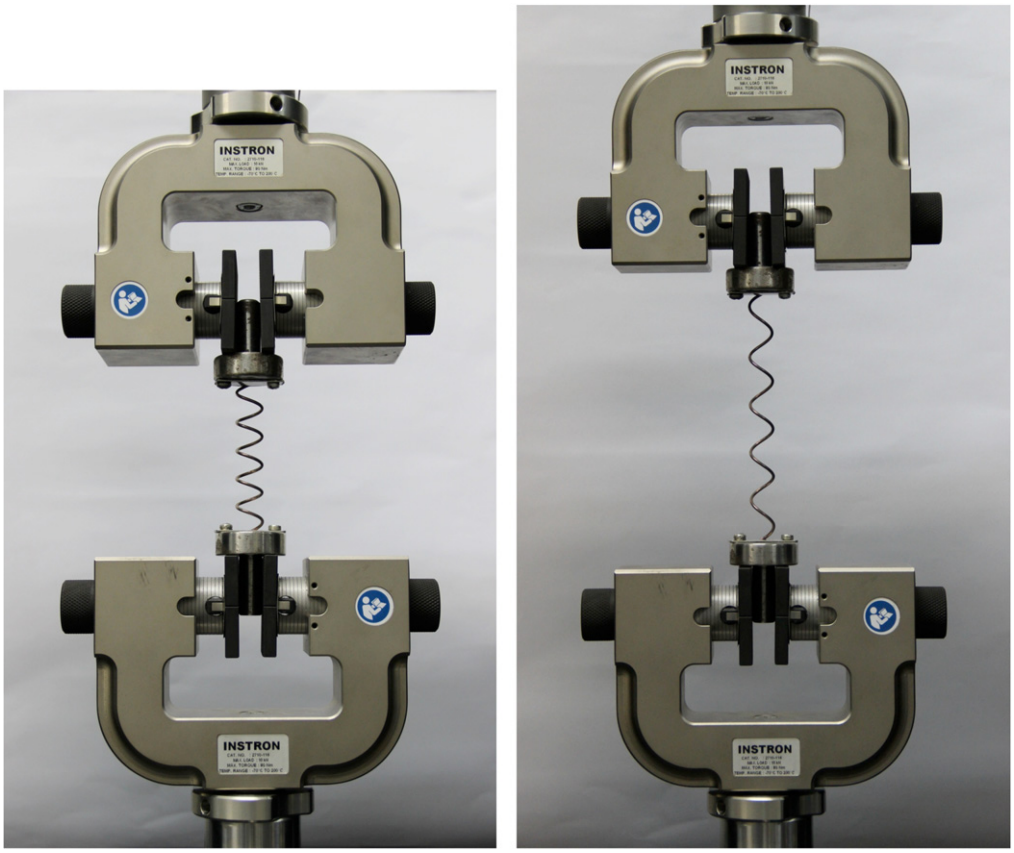

(a) (b)

Figure 5. S-Spring test at the maximum displacement configuration: (a) 65 mm, (b) 120 mm.

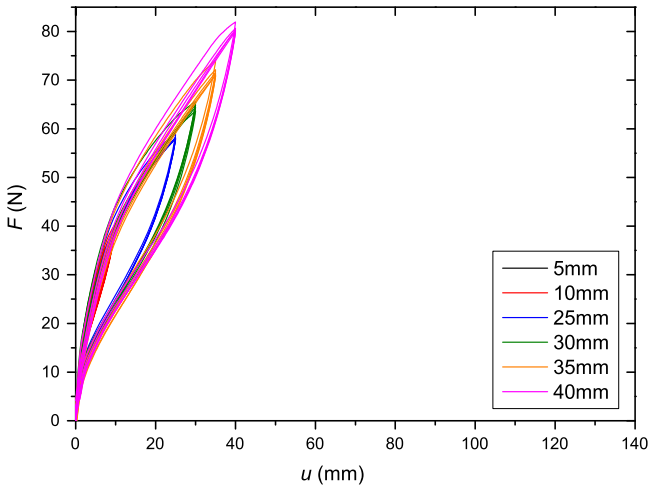

Figure 6. Force-displacement curves of the W-Spring.

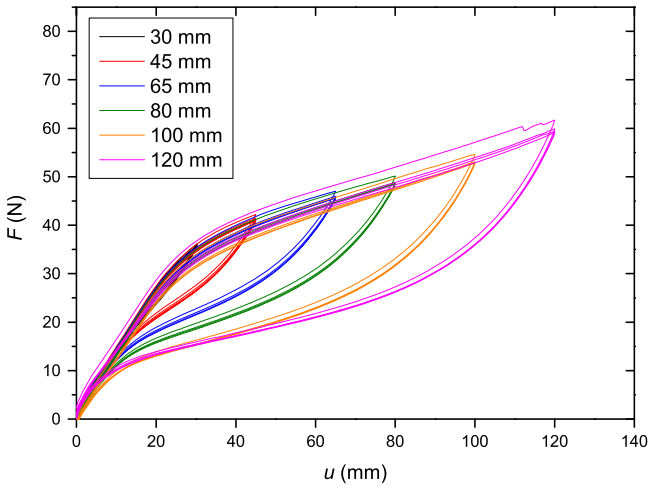

Figure 7. Force-displacement curve of the S-Spring.

Table 3. Stiffness estimation of the W-Spring.

Displacements (mm)	5	10	25	30	35	40	Average
K_A (N mm^{-1})	9.9	9.5	9.3	8.8	8.5	8.0	9.0
K_M (N mm^{-1})	4.9	4.3	4.1	4.2	4.4	4.6	4.4

behavior in terms of the definition of stiffness as the slope of the curve. Note that the austenitic stiffness, which is calculated from the slope of the austenitic region, is generally smaller than the martensitic stiffness calculated from the slope of the martensitic region. Table 4 presents the summary of the stiffness, showing the average values of $\bar{K}_A = 1.2$ N mm^{-1} and $\bar{K}_M = 1.5$ N mm^{-1}. This represents an increase of around

Table 4. Stiffness estimation of the S-Spring.

Displacements (mm)	30	45	65	80	100	120	Average
K_A (N mm^{-1})	1.3	1.4	1.2	1.2	1.2	1.0	1.2
K_M (N mm^{-1})	1.3	1.3	1.4	1.4	1.6	1.7	1.5

20%. Since the austenitic shear modulus is larger than the martensitic one, the geometric nonlinearity is responsible for this change.

4. Finite element analysis

Numerical simulations promote a proper explanation of the experimental observations. A three-dimensional finite element model is used to study the pseudoelastic behavior of SMA helical springs subjected to axial loadings. Geometrical nonlinearities are included in the analysis, considering a large displacement hypothesis. A commercial finite element code ANSYS is employed considering coupled thermal and mechanical fields. Element SOLID 186 is chosen to perform spatial discretization.

Constitutive nonlinearity is related to the SMA's thermomechanical behavior, and different constitutive models can be used for this description. Lagoudas (2008) and Paiva and Savi (2006) presented an overview of constitutive models for SMAs. Here, the constitutive model proposed by Auricchio *et al* (1997) is used. This three-dimensional model can describe the pseudoelastic behavior considering both the austenite (A) and martensite (M) phases. The internal variables, ξ_A and ξ_M, are introduced to represent, respectively, austenitic and martensitic volume fractions that satisfy the relation $\xi_A + \xi_M = 1$. Hence, it is possible to use only one internal variable, $\xi = \xi_M = 1 - \xi_A$. Under these assumptions, the constitutive relation is given by:

$$\boldsymbol{\sigma} = \mathbf{E}\colon (\boldsymbol{\varepsilon} - \boldsymbol{\varepsilon}_{tr}) \tag{2}$$

$$\dot{\boldsymbol{\varepsilon}}_{tr} = \dot{\xi}\, \varepsilon_L \frac{\partial P}{\partial \boldsymbol{\sigma}} \tag{3}$$

where $\mathbf{E}$ is the elastic tensor, $\boldsymbol{\varepsilon}_{tr}$ is the transformation strain tensor, and ε_L represents a parameter associated with recoverable strain resulting from martensitic phase transformation. Isotropic assumption is adopted, and the phase transformation obeys a Drucker-Prager loading function, P. The elastic behavior for the austenite and martensite phases is related to Young's modulus (E) and the Poisson ratio (ν). The process of phase transformation is controlled by four critical stresses —σ_s^{AM}, σ_f^{AM}, σ_s^{MA}, and σ_f^{MA}—where the s and f subscripts stand for start and finish, AM represents the austenite-martensite transformation, and MA represents the martensite-austenite transformation. The following relations define phase transformations:

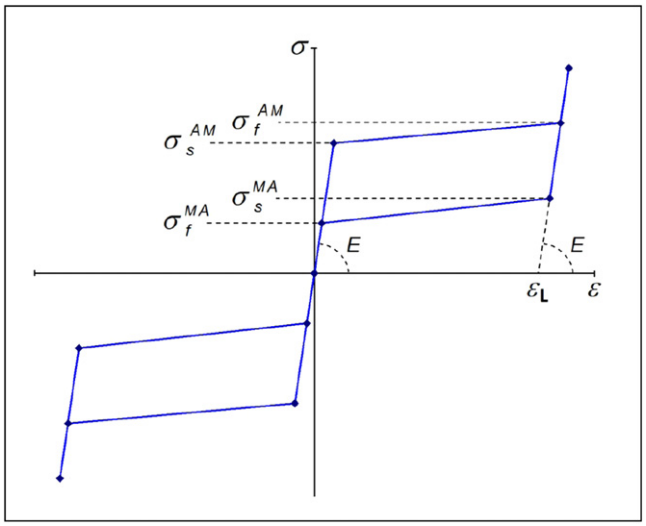

Figure 8. Idealized one-dimensional stress-strain curve for the pseudoelastic behavior described by the model of Auricchio *et al* (1997).

$$\dot{\xi} = \begin{cases} -H^{AM}(1-\xi)\dfrac{\dot{P}}{P - R_f^{AM}} \\ H^{MA}\xi\dfrac{\dot{P}}{P - R_f^{MA}} \end{cases} \tag{4}$$

where $R_f^{AM} = \sigma_f^{AM}(1+\alpha)$ and $R_f^{MA} = \sigma_f^{MA}(1+\alpha)$. In addition, it is important to define:

$$H^{AM} = \begin{cases} 1 \text{ if } R_s^{AM} < P < R_f^{AM} \text{ and } \dot{P} > 0 \\ 0 \text{ otherwise} \end{cases} \tag{5}$$

$$H^{MA} = \begin{cases} 1 \text{ if } R_s^{MA} < P < R_f^{MA} \text{ and } \dot{P} < 0 \\ 0 \text{ otherwise} \end{cases}. \tag{6}$$

Figure 8 presents a one-dimensional stress-strain curve related to the pseudoelastic behavior described by the model by Auricchio *et al* (1997). It is important to highlight that this model uses the same Young's modulus for both the austenite and martensite phases. Based on this restriction, all simulations are performed assuming the austenitic Young's modulus.

Although this model cannot describe all the complex details of the SMA's thermomechanical behavior, it is convenient for several purposes because it allows the description of important features used in the design of SMA devices. Several authors have adopted similar hypotheses to successfully model SMA behavior (Abeyaratne and Kim 1994, Brocca *et al* 2002, Sadjadpour and Bhattacharya 2007, Zhu and Zhang 2007, Auricchio *et al* 2007, Kadkhodaei *et al* 2008). Indeed, despite the limitations of the model used in this work, comparisons with experimental data show that this SMA model properly captures the main behavior of a pseudoelastic helical spring subjected to mechanical loadings.

Numerical simulations are performed by considering parameters presented in table 5. In essence, these values are

Table 5. SMA mechanical parameters.

Mechanical properties	Value
E (GPa)	46
ν	0.30
σ_s^{AM} (MPa)	297
σ_f^{AM} (MPa)	772
σ_s^{MA} (MPa)	306
σ_f^{MA} (MPa)	78
ε_L	0.07

adjusted using the experimental data described in the preceding section.

The finite element analysis is carried out considering a solid model (shown in figure 9) that represents both the W-Spring and the S-Spring with a mesh obtained after a convergence analysis. Experimental situations are reproduced by considering proper boundary conditions involving displacement restrictions and loadings. Basically, it is assumed that one end of the spring is fixed, prescribing null displacements for all degrees of freedom on its cross section area. The other end's cross section is subjected to a prescribed load-unload cyclic displacement in the spring's longitudinal direction. Variables' distribution through the spring, as stress and volume fractions, are analyzed at a central section to avoid the effects of the loadings and the prescribed boundary conditions at the spring's two ends.

Initially, a calibration process is developed to adjust the model parameters presented in table 5. Figure 10 shows a comparison between numerical and experimental data considering 4 loading conditions of the W-Spring. Similar comparisons related to the S-Spring are presented in figure 11. Results show that model simulations capture the general behavior observed in the experimental data. Note that since the constitutive SMA model considers the same Young's modulus for both the austenitic and martensitic phases, numerical simulations have this restriction and do not capture the stiffness change. Nevertheless, results show that the

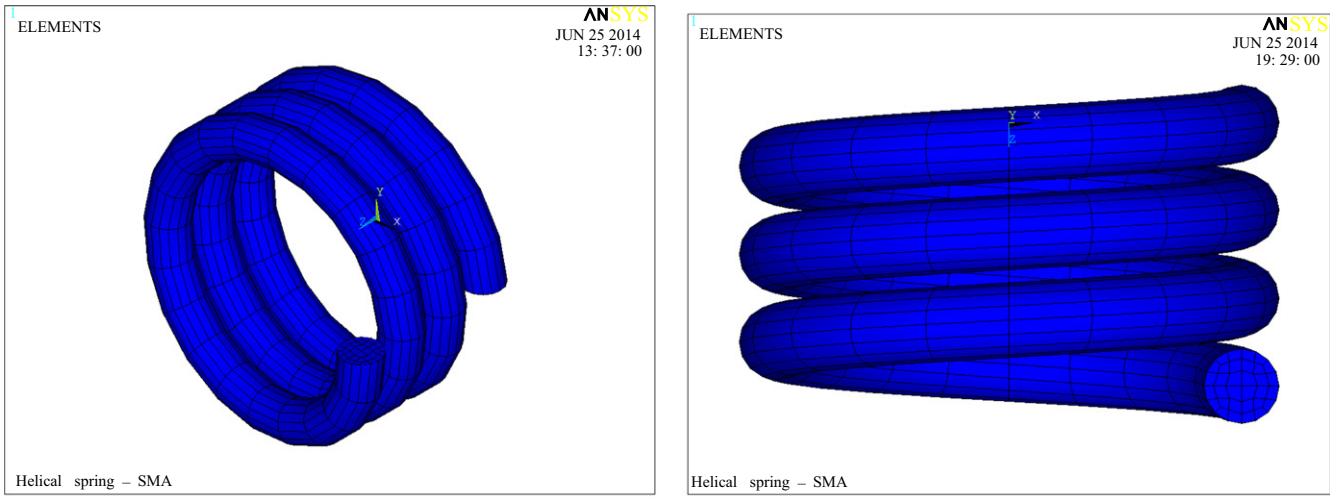

(a)

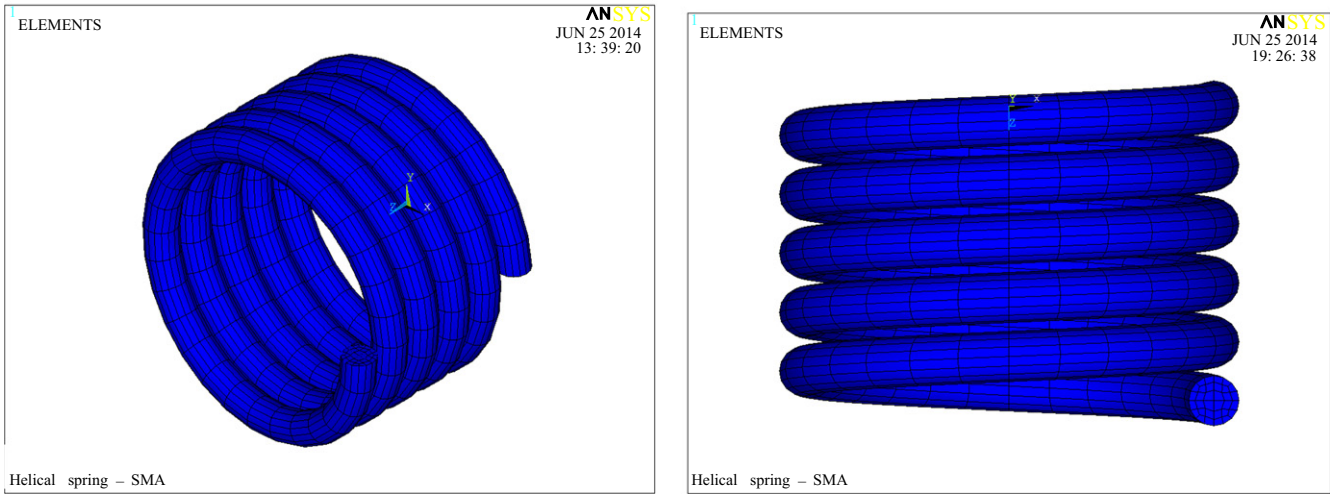

(b)

Figure 9. SMA helical spring finite element mesh. (a) W-Spring. (b) S-Spring.

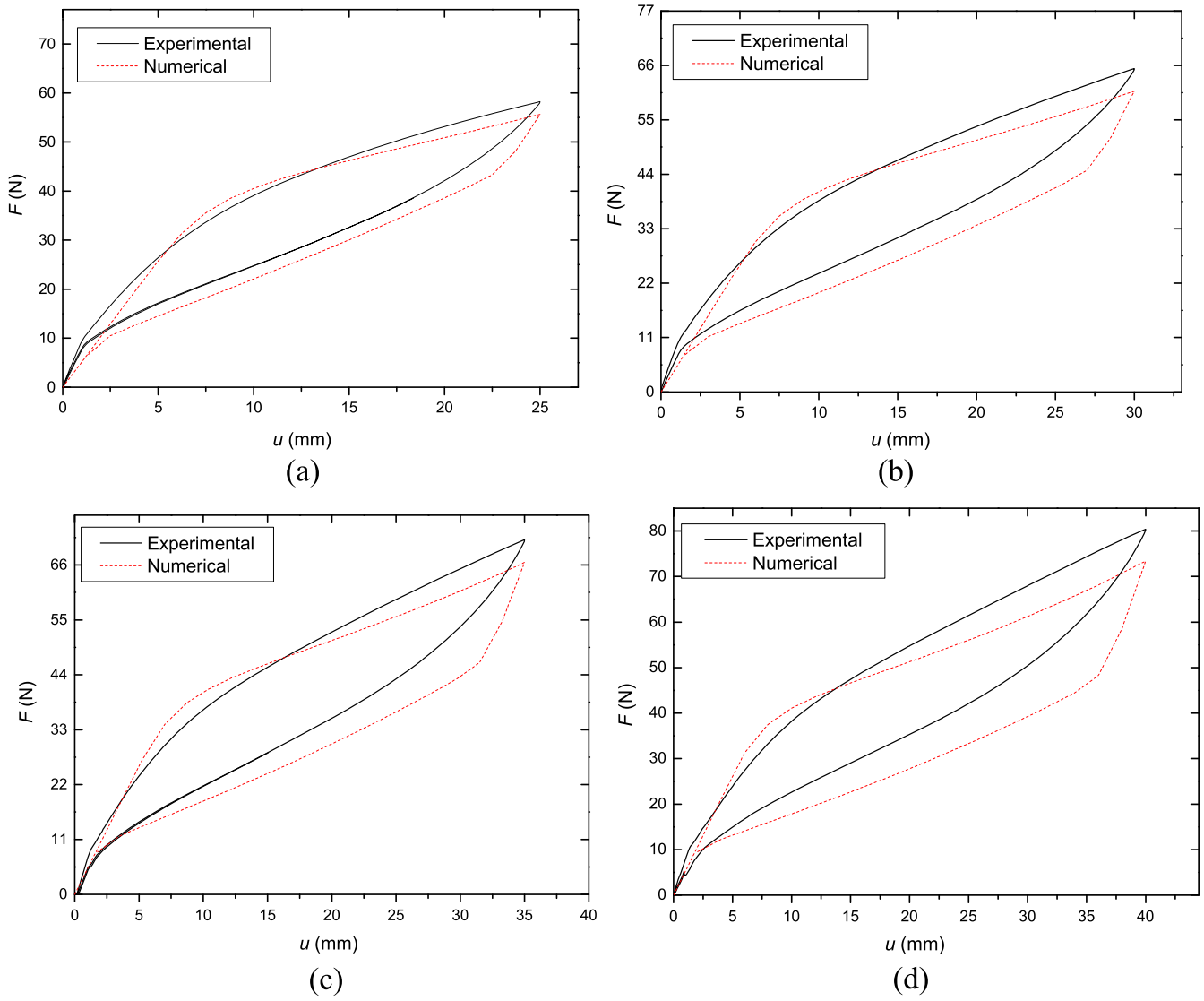

Figure 10. Experimental and numerical load-displacement curves for cyclic tests of the W-Spring. Maximum displacement of (a) 25 mm, (b) 30 mm, (c) 35 mm, and (d) 40 mm.

proposed model can represent the behavior of the SMA helical spring.

After the model adjustment, numerical simulations are performed to show the influence of the geometrical non-linearities. The maximum displacements of the previous results are treated as follows: the W-Spring with 40 mm of maximum prescribed displacement, and the S-Spring with 120 mm of maximum prescribed displacement. To establish a proper comparison between both springs, two situations are chosen that analyze similar values of stresses and volume fractions. Figure 12 shows SMA helical springs in initial and deformed configurations for both springs. As observed in the experimental analysis, SMA helical springs are subjected to large displacements. The W-Spring has an initial length of approximately 6 mm and hence, the 40 mm maximum value of prescribed displacement represents eight times the original length. On the other hand, the S-Spring has an initial length of approximately 10 mm, and therefore the spring is subjected to a twelve-fold increase of its initial length.

Figure 13 shows the von Mises equivalent stress distribution, while figure 14 shows the martensitic volume fraction for the two situations. Under these assumptions, the differences between both springs are smaller than 3% (von Mises equivalent stress of 600 MPa and martensitic volume fraction of 62%, approximately). The results show just the central coils, avoiding the boundary effects by removing the two end coils. The stress field presents a typical distribution of helical springs, which is associated with a combination of shear internal loads acting in the cross section. Since a torque in cylindrical bodies promotes a shear stress distribution with zero values at the center and maximum values at the surface, values of either the von Mises equivalent stress or the martensitic volume fraction are maximum at the cylinder surface. Nevertheless, it is important to note that equivalent stresses and the martensitic volume fraction distribution along the wire diameter do not present a symmetrical distribution. This is a consequence of the curvature effect, and higher values of

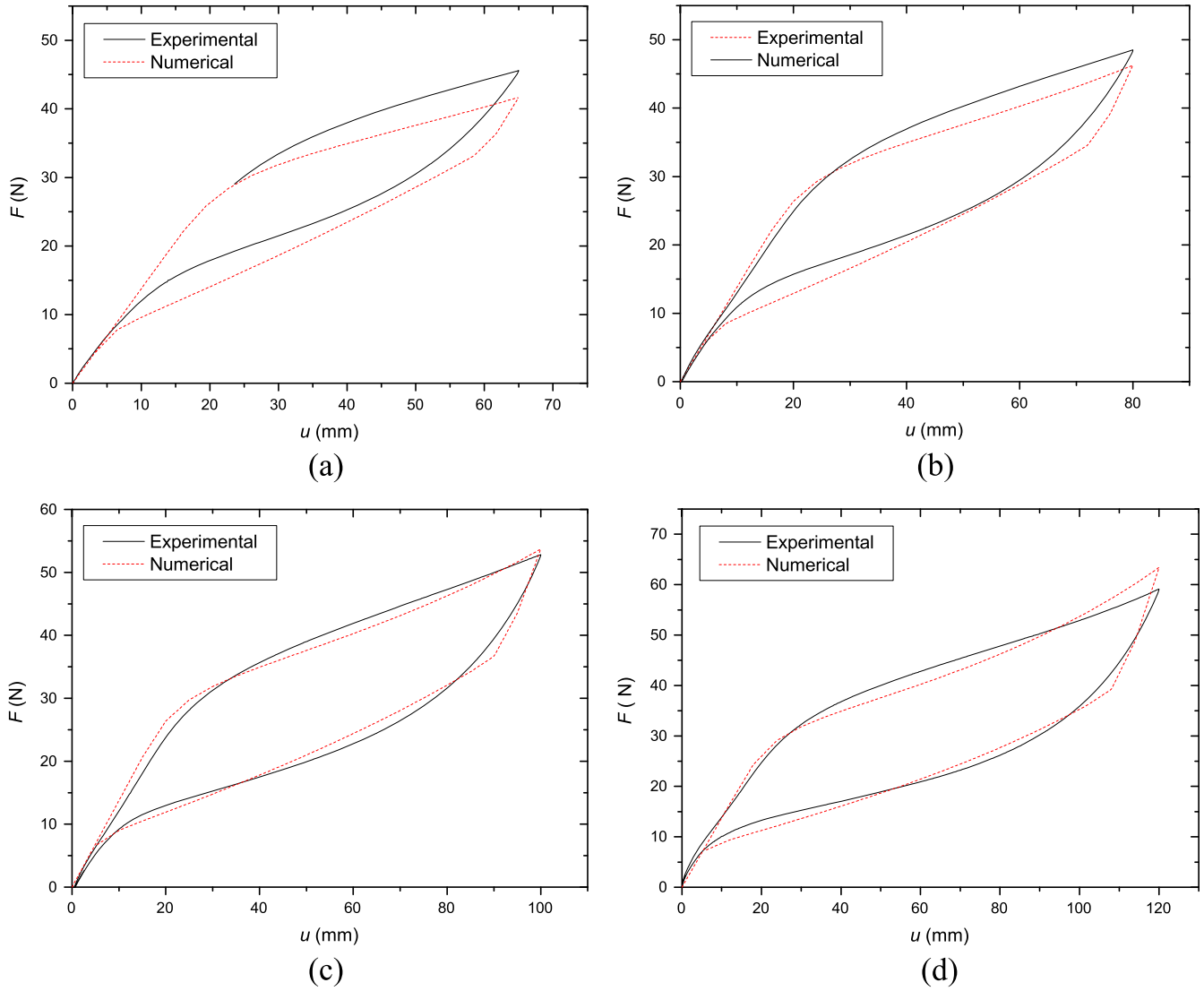

Figure 11. Experimental and numerical load-displacement curves for cyclic tests of the S-Spring. Maximum displacement of (a) 65 mm, (b) 80 mm, (c) 100 mm, and (d) 120 mm.

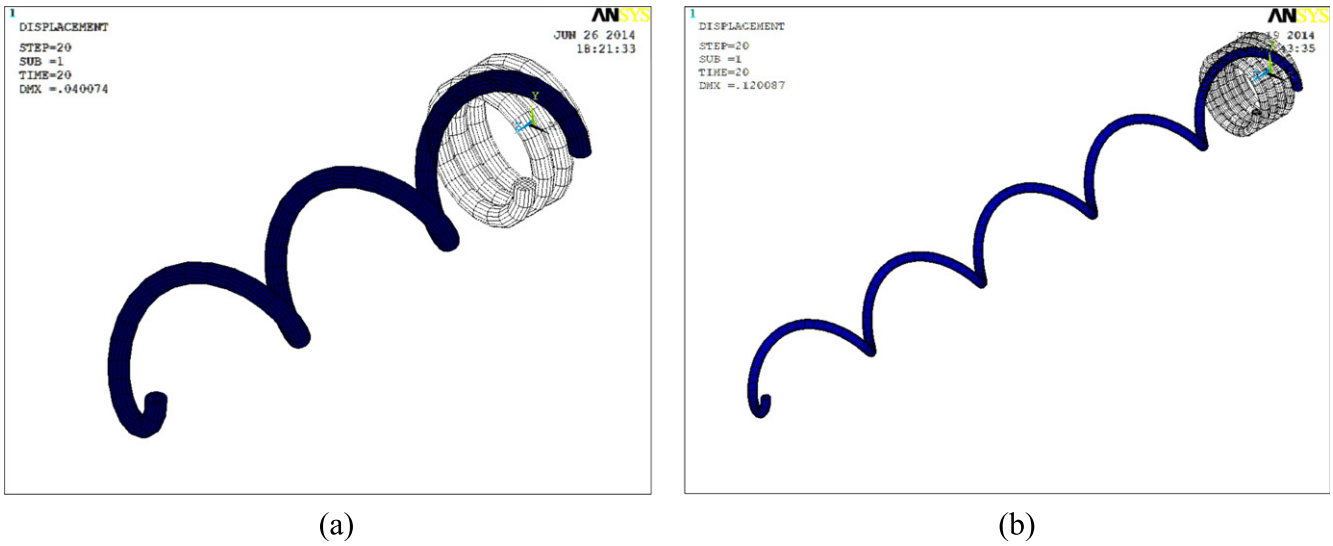

Figure 12. SMA helical spring, initial and deformed configurations: (a) W-Spring (40 mm maximum displacement), and (b) S-Spring (120 mm maximum displacement).

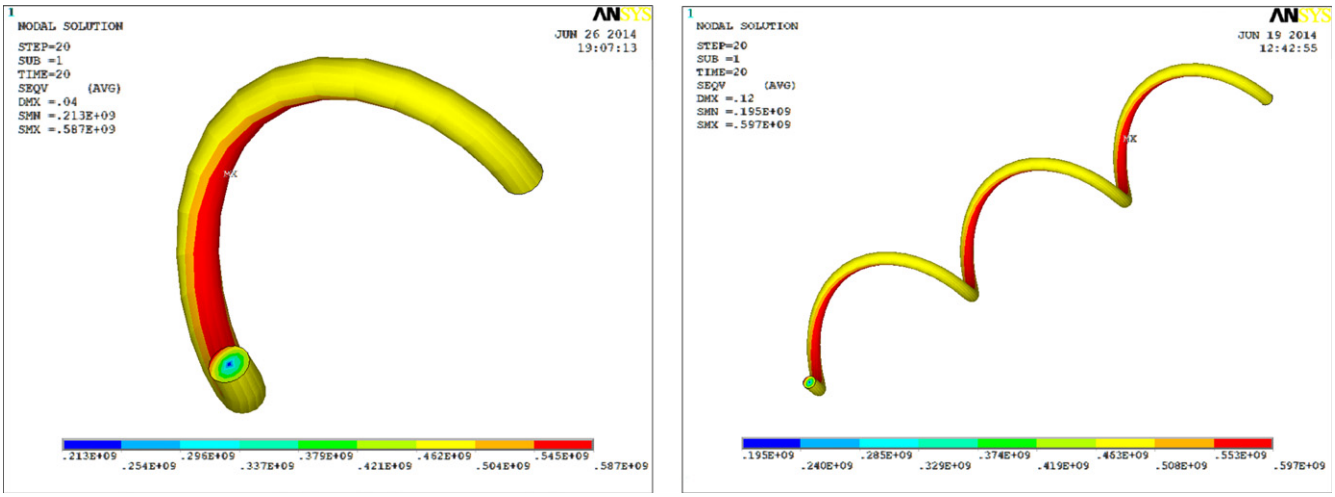

(a) (b)

Figure 13. von Mises equivalent stress distribution: (a) W-Spring (40 mm maximum displacement), and (b) S-Spring (120 mm maximum displacement).

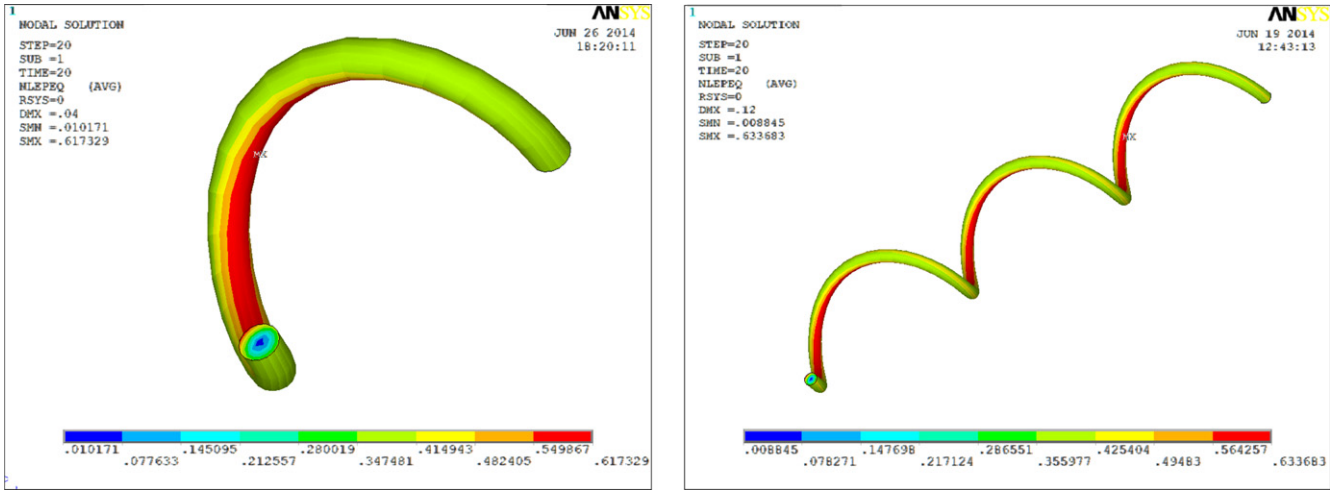

(a) (b)

Figure 14. Martensitic volume fraction distribution: (a) W-Spring (40 mm maximum displacement), and (b) S-Spring (120 mm maximum displacement).

stresses and the martensitic volume fraction are observed near the spring's longitudinal axis (Mirzaeifar *et al* 2011).

The effect of geometric nonlinearity is now of concern. A comparison between numerical results considering two distinct models is performed: the geometric linear (GL) model, neglecting nonlinear geometrical effects; and the geometrical nonlinear (GNL) model. This can be achieved through the NLGEOM command in the ANSYS computational package. Once again, it is important to point out that the SMA constitutive model does not consider a different Young's modulus for the austenite and martensite phases. Therefore, the model does not capture the stiffness change observed in experimental tests. Nevertheless, the model has a good agreement with the experimental data, making it an appropriate tool to evaluate the effect of geometric nonlinearities in the spring's stiffness. Figure 15 shows the results for both springs, considering both models for each spring. The W-Spring analysis adopts a maximum prescribed displacement of 64 mm. On the other hand, the S-Spring analysis adopts a value of 175 mm. Under these assumptions, for the GNL model, both springs present maximum values of von Mises equivalent stress and a martensitic volume fraction of 1280 MPa and 100%, respectively. It is clear that geometric nonlinearities induce changes in the martensitic phase, reaching situations observed in experimental tests. This is evident when observing that the S-Spring has more pronounced changes in spring stiffness when compared with the W-Spring, which is exactly what the experimental tests revealed.

Since the spring index (C) is usually used to quantify the effect of the geometric nonlinearity, one can now focus on numerical simulations considering different indexes. The idea

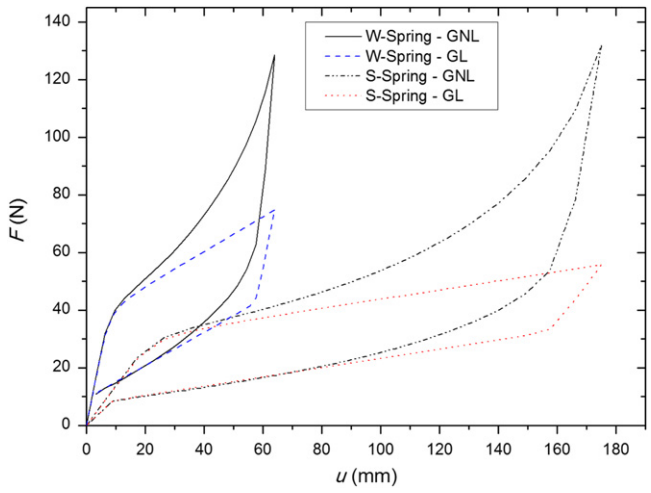

Figure 15. Effect of the geometric nonlinearities for the W-Spring and S-Spring, considering the GL and NGL models.

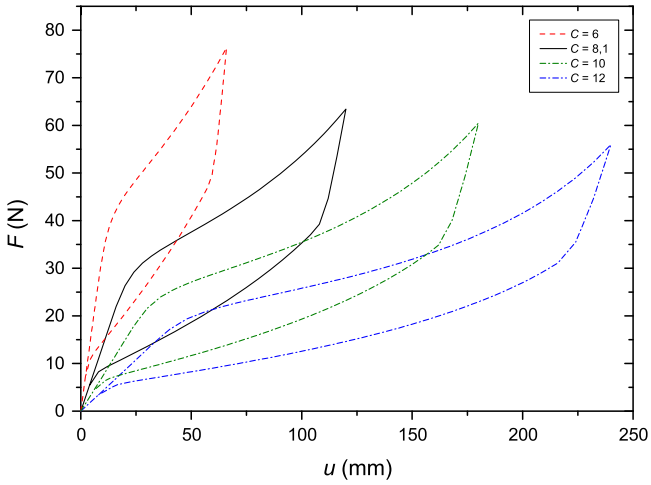

Figure 16. Effect of the spring index on the geometric nonlinearities: force-displacement curves.

is to define the S-Spring as a reference ($d = 1.7$ mm; $D = 13.8$ mm; $N = 5$), giving a situation with a spring index of

Table 6. Effect of spring index on the geometric nonlinearities.

C	K_A (N m^{-1})	K_M (N m^{-1})	K_M/K_A
6	3422	4812	1.4
8.1	1375	2471	1.8
10	742	1848	2.5
12	219	1434	6.6

$C = 8.1$. Three other springs with different spring indexes are treated, considering the variation of the external diameters. Therefore, four spring indexes are investigated: 6, 8.1 (S-Spring), 10, and 12. Figure 16 presents results related to these four situations with similar loading levels (maximum values for von Mises equivalent stress and martensitic volume fraction of approximately 600 MPa and 62%, respectively). Note that the increase of the spring index, C, tends to increase the stiffness variation, represented by the ratio K_M/K_A. The larger index values are associated with stronger geometric nonlinearity effects. Therefore, the larger geometric nonlinear effects are present in the spring with the larger C value (12). Figure 17 shows this variation, while table 6 presents the calculated values.

5. Conclusions

This paper investigates the nonlinear geometric effect on the mechanical behavior of SMA helical springs. Initially, characterization of the SMA wires was presented. Then, the design and manufacturing of SMA springs was discussed. Experimental tensile tests were then carried out to show the nonlinear geometric influence. Results showed the change of austenitic and martensitic stiffness due to geometric influence. Two different springs were built from SMA wires, defining a spring with weak nonlinear geometric influence, called the W-Spring, and another one with a strong nonlinear geometric influence, called the S-Spring. Tensile tests show that the W-Spring has $K_A > K_M$, while the S-Spring presents $K_A < K_M$. Since the shear modulus is $G_A > G_M$ for both cases, this

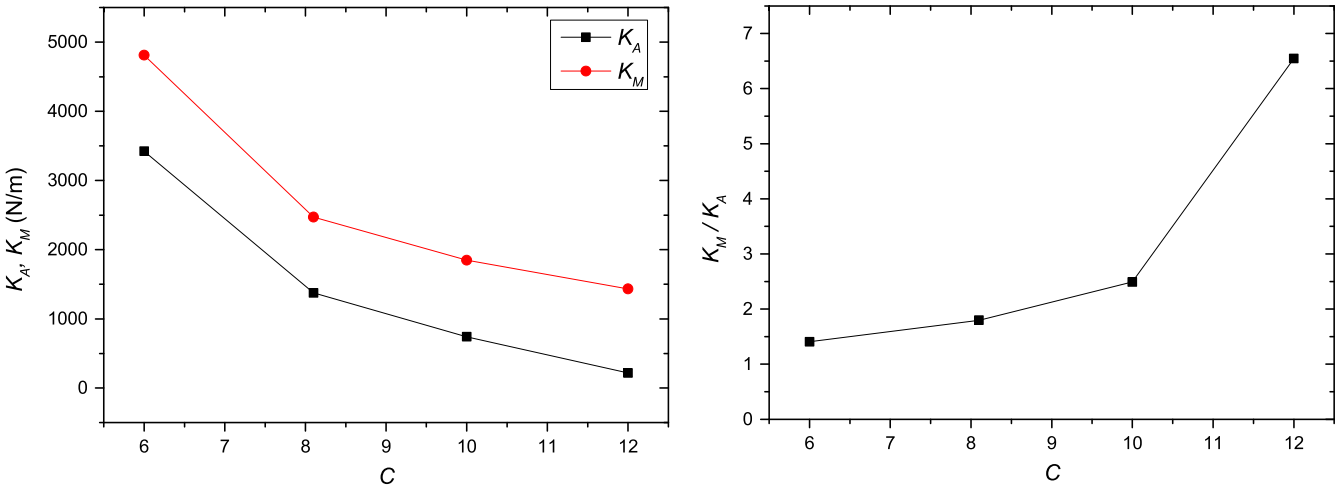

Figure 17. Effect of the spring index on the geometric nonlinearities: stiffness changes.

difference is due to geometrical nonlinearities. Finite element analysis was performed to confirm this general conclusion. GL and NGL models were used for this analysis. Results confirmed conclusions obtained from experimental data. In addition, an analysis related to the spring index showed how the geometric nonlinearity can be quantified. On this basis, it is important to contemplate the coupling between constitutive and geometric nonlinearities in the design of SMA helical springs.

Acknowledgments

The authors would like to acknowledge the support of the Brazilian Research Agencies CNPq, CAPES, and FAPERJ, and through the INCT-EIE, (National Institute of Science and Technology—Smart Structures in Engineering) the CNPq and FAPEMIG. We also acknowledge the Air Force Office of Scientific Research (AFOSR).

References

Abeyaratne R and Kim S-J 1994 A one-dimensional continuum model for shape-memory alloys *Int. J. Solids Struct.* **31** 2229–49

Aguiar R A A, Savi M A and Pacheco P M C L 2010 Experimental and numerical investigations of shape memory alloy helical springs *Smart Mater. Struct.* **19** 025008

Attanasi G, Auricchio F and Urbano M 2011 Theoretical and experimental investigation on SMA superelastic springs *J. Mater. Eng. Perform.* **20** 706–11

Auricchio F, Reali A and Stefanelli U 2007 A three-dimensional model describing stress-induced solid phase transformation with permanent inelasticity *Int. J. Plast.* **23** 207–26

Auricchio F, Taylor R L and Lubliner J 1997 Shape-memory alloys: macromodeling and numerical simulations of the superelastic behavior *Computational Methods in Applied Mechanical Engineering* **146** 281–312

Brocca M, Brinson L C and Bazant Z P 2002 Three-dimensional constitutive model for shape memory alloys based on microplane model *J. Mech. Phys. Solids* **50** 1051–77

Bundhoo V, Haslam E, Birch B and Park E J 2009 A shape memory alloy-based tendon-driven actuation system for biomimetic artificial fingers: I. Design and evaluation *Robotica* **27** 131–46

Follador M, Cianchetti M and Laschi C 2012 A general method for the design and fabrication of shape memory alloy active spring actuators *Smart Mater. Struct.* **21** 115029 10

Hartl D J, Lagoudas D C, Calkins F T and Mabe J H 2010 Use of a Ni60Ti shape memory alloy for active jet engine Chevron application: I. Thermomechanical characterization *Smart Mater. Struct.* **19** 015020

Hartl D J, Lagoudas D C, Calkins F T and Mabe J H 2010a Use of a Ni60Ti shape memory alloy for active jet engine Chevron application: II. Experimentally validated numerical analysis *Smart Mater.Struct.* **19** 015021

Jee K K, Han J H, Kim Y B, Lee D H and Jang W Y 2008 New method for improving properties of SMA coil springs *Eur. Phys. J. Special Topics* **158** 261–6

Kadkhodaei M, Salimi M, Rajapakse R K N D and Mahzoon M 2008 Modeling of shape memory alloys based on microplane theory *J. Intell. Mater. Sys. Struct.* **19** 541–50

Lagoudas D C 2008 *Shape Memory Alloys—Modeling and Engineering Applications* (Berlin: Springer)

Liang C and Rogers C A 1997 Design of shape memory alloy springs with applications in vibration control *J. Intell. Mater. Sys. Struct.* **8** 314–22

Machado L G and Savi M A 2003 Medical applications of shape memory alloys *Brazilian Journal of Medical and Biological Research* **36** 683–91

Marketz F and Fischer F D 1994 A Micromechanical study on the coupling effect between microplastic deformation and martensitic transformation *Comput. Mater. Sci.* **3** 307–25

Min An S, Ryu J, Cho M and Cho K J 2012 Engineering design framework for a shape memory alloy coil spring actuator using a static two-state model *Smart Mater. Struct.* **21** 055009

Mirzaeifar R, DesRoches R and Yavari A 2011 A combined analytical, numerical, and experimental study of shape-memory-alloy helical springs *Int. J. Solids Struct.* **48** 611–24

Morgan N B and Broadley M 2004 Taking the art out of smart!—forming processes and durability issues for the application of NiTi shape memory alloys in medical devices *Proc. of the Materials and Processes for Medical Devices Conf. (Anaheim)* pp 247–52

Paiva A and Savi M A 2006 An overview of constitutive models for shape memory alloys *Math. Prob. Eng.* **2006** 1–30

Paiva A, Savi M A, Braga A M B and Pacheco P M C L 2005 A constitutive model for shape memory alloys considering tensile-compressive asymmetry and plasticity *Int. J. Solids Struct.* **42** 3439–57

Sadjadpour A and Bhattacharya K 2007 A micromechanics inspired constitutive model for shape-memory alloys: the one-dimensional case *Smart Mater. Struct.* **16** S51–62

Shigley J E and Mischke 2001 *Mechanical Engineering Design* (New York: McGraw Hill)

Speicher M, Hodgson D E, DesRooches R and Leon R T 2009 Shape memory alloy tension/compression device for seismic retrofit of buildings *J. Mater. Eng. Perform.* **18** 746–53

Spinella I and Dragoni E 2010 Analysis and design of hollow helical springs for shape memory actuators *J. Intell. Mater. Sys. Struct.* **21** 185–99

Sung-Min A, Junghyun R, Maenghyo C and Kyu-Jin C 2012 Engineering design framework for a shape memory alloy coil spring actuator using a static two-state model *Smart Mater. Struct.* **21** 055009 16

Tobushi H and Tanaka K 1991 Deformation of a shape memory alloy helical spring *JSME Int. J.* Series I **34** 83–9

Toi Y, Lee J B and Taya M 2004 Finite element analysis of superelastic, large deformation behavior of shape memory alloy helical spring *Comput. Struct.* **82** 1685–93

Wu M H 2001 Fabrication of nitinol materials and components *Proc. of the Int. Conf. on Shape memory and Superelastic Technologies (Kunming, China)* pp 285–92

Zhu S and Zhang Y 2007 A thermomechanical constitutive model for superelastic SMA wire with strain-rate dependence *Smart Mater. Struct.* **16** 1696–707